## Methods

The growth experiments were carried out in a Philips CM300 FEG TEM equipped with an *in situ* cell[13]. This system provides images with a resolution better than 0.14 nm of samples exposed to reactive gases and elevated temperatures. A Tietz FastScan-F114 CCD was used for recording TEM images. The image acquisition time was adjusted to suit the reshaping of the Ni nanocrystals and ranged from 2 to 10 frames $s^{-1}$. A total of 16 video sequences (each consisting of 300–1,200 consecutive high-resolution images) showing the coupling of graphene growth to Ni step-edge dynamics were recorded in six different growth experiments. The electron beam intensity was kept in the interval 0.2–2 A $cm^{-2}$, which was sufficiently low to avoid any influence of the electron beam on the growth. Growth experiments with the electron beam switched off resulted in the same carbon nanofibre structures as in the low-dose *in situ* experiments.

The self-consistent DFT calculations were performed using the LDA[14] or the GGA-RPBE approximation[16] for exchange and correlation. The interaction of the graphene overlayer with the Ni(111) surface was dominated by van der Waals forces. The LDA for the exchange and correlation term is known to give the best description of such weak interactions[24]. We have therefore used LDA for calculating the adsorption energy and diffusion energy barrier for C and Ni adatoms on the clean Ni(111) surface and the graphene–Ni(111) interface. The adsorption energies and diffusion energy barriers on the clean Ni(111) surface calculated by the GGA-RPBE approximation were found to be essentially the same. However, within the GGA-RPBE approximation we found no adhesion of the graphene overlayer to the Ni(111) surface.

The ionic cores are described by ultrasoft pseudopotentials[25] and the one-electron valence states were expanded in a basis of plane waves with kinetic energy below 25 Ry. The electron density was determined self-consistently by iterative diagonalization of the Kohn–Sham hamiltonian, Pulay mixing[26] of the resulting electronic density and Fermi occupation of the Kohn–Sham states ($k_BT = 0.1$ eV). All total energy calculations were extrapolated to zero electronic temperature and performed with the magnetic moment of the nickel surface taken into account.

The Ni(111) surface was modelled by a periodic repetition of a three-layer slab, whereas a slab thickness of nine layers was used in the [211] direction to create a stepped surface and a thickness comparable to the Ni(111) surface. In both cases, the slabs were separated by ~10 Å of vacuum. In the Ni(111) model, the top layer was allowed to fully relax, whereas in the Ni(211) model, the uppermost close-packed (111) layer was relaxed fully. The remaining layers were kept fixed in the bulk geometry with a calculated equilibrium lattice constant of 3.52 Å. For all calculations on Ni(111), a p(2 × 2) lateral unit cell was used, giving C and Ni adsorbate coverages of 0.25 ML, whereas the C/Ni ratio for the graphene overlayer was 2. For the Ni(211) surface, a (1 × 2) unit cell was used in the calculations with a one-to-one coverage of adsorbate to Ni step edge atoms. A sampling of 4 × 4 × 1 Monkhorst–Pack special *k*-points was used, resulting in 8 *k*-points in the irreducible Brillouin zone.

Received 20 August; accepted 5 December 2003; doi:10.1038/nature02278.


1. Baughman, R. H., Zakhidov, A. A. & de Heer, W. A. Carbon nanotubes—the route towards applications. *Science* **297,** 787–792 (2002).
2. Ajayan, P. M. Nanotubes from carbon. *Chem. Rev.* **99,** 1787–1799 (1999).
3. Rostrup-Nielsen, J. R., Sehested, J. & Nørskov, J. K. Hydrogen and synthesis gas by steam and $CO_2$ reforming. *Adv. Catal.* **47,** 65–138 (2002).
4. Ebbesen, T. W. & Ajayan, P. M. Large-scale synthesis of carbon nanotubes. *Nature* **358,** 220–222 (1992).
5. Thess, A. *et al.* Crystalline ropes of metallic carbon nanotubes. *Science* **273,** 483–487 (1996).
6. Kong, J., Soh, H. T., Cassell, A. M., Quate, C. F. & Dai, H. Synthesis of individual single-walled carbon nanotubes on patterned silicon wafers. *Nature* **395,** 878–881 (1998).
7. Boskovic, B. O. *et al.* Large-area synthesis of carbon nanofibres at room temperature. *Nature Mater.* **1,** 165–168 (2002).
8. Baker, R. T. K., Harris, P. S., Thomas, R. B. & Waite, R. J. Nucleation and growth of carbon deposits from the nickel catalyzed decomposition of acetylene. *J. Catal.* **26,** 51–62 (1972).
9. Rostrup-Nielsen, J. R. Equilibria of decomposition reactions of carbon monoxide and methane over nickel catalysts. *J. Catal.* **27,** 343–356 (1972).
10. Charlier, J.-C. & Iijima, S. in *Growth Mechanisms of Carbon Nanotubes* (eds Dresselhaus, M. S., Dresselhaus, G. & Avouris, Ph.) Vol. 80, *Topics in Applied Physics* 55–80 (Springer, Heidelberg, 2001).
11. Clausen, B. S., Topsøe, H. & Frahm, R. Application of combined X-ray diffraction and absorption techniques for *in situ* catalyst characterisation. *Adv. Catal.* **42,** 315–344 (1998).
12. Topsøe, H. *In situ* characterisation of catalysts. *Stud. Surf. Sci. Catal.* **130,** 1–21 (2000).
13. Hansen, P. L. *et al.* Atom-resolved imaging of dynamic shape changes in supported copper nanocrystals. *Science* **295,** 2053–2055 (2002).
14. Jones, R. O. & Gunnarsson, O. The density functional formalism, its applications and prospects. *Rev. Mod. Phys.* **61,** 689–746 (1989).
15. Rosei, R. *et al.* Structure of graphitic carbon on Ni(111): A surface extended-energy-loss fine-structure study. *Phys. Rev. B* **28,** 1161–1164 (1983).
16. Hammer, B., Hansen, L. B. & Nørskov, J. K. Improved adsorption energetics within density-functional theory using revised Perdew-Burke-Ernzerhof functionals. *Phys. Rev. B* **59,** 7413–7421 (1999).
17. Bengaard, H. S. *et al.* Steam reforming and graphite formation in Ni catalysts. *J. Catal.* **209,** 365–384 (2002).
18. Trimm, D. L. The formation and removal of coke from nickel catalyst. *Catal. Rev. Sci. Eng.* **16,** 155–189 (1977).
19. Alstrup, I. A new model explaining carbon filament growth on nickel, iron and Ni-Cu alloy catalysts. *J. Catal.* **109,** 241–251 (1988).
20. Rostrup-Nielsen, J. R. & Trimm, D. L. Mechanisms of carbon formation on nickel-containing catalysts. *J. Catal.* **48,** 155–165 (1977).
21. De Jong, K. P. & Geus, J. W. Carbon nanofibers: catalytic synthesis and applications. *Catal. Rev. Sci. Eng.* **42,** 481–510 (2000).
22. Askeland, D. R. *The Science and Engineering of Materials* 2nd edn, Ch. 5 (PWS-KENT, Boston, 1989).
23. Nørskov, J. K. *et al.* Universality in heterogeneous catalysis. *J. Catal.* **209,** 275–278 (2002).
24. Da Silva, J. L. F., Stampfl, C. & Scheffler, M. Adsorption of Xe atoms on metal surfaces: new insights from first-principles calculations. *Phys. Rev. Lett.* **90,** 066104 (2003).
25. Vanderbilt, D. H. Soft self-consistent pseudopotentials in a generalized eigenvalue formalism. *Phys. Rev. B* **41,** 7892–7895 (1990).
26. Kresse, G. & Forthmüller, J. Efficiency of *ab-initio* total energy calculations for metals and semiconductors using a plane-wave basis set. *Comput. Mater. Sci.* **6,** 15–50 (1996).


**Supplementary Information** accompanies the paper on **www.nature.com/nature**.

**Acknowledgements** We gratefully acknowledge the participation of the CTCI Foundation, Taiwan, in the establishment of the TEM facility at Haldor Topsøe A/S. S.H. acknowledges support from the Danish Research Council, STVF. F.A.P. and J.K.N. acknowledge computational resources from the Danish Center for Scientific Computing. C.L.-C. acknowledges support from Facultad de Ciencias, Universidad de Cádiz, Puerto Real, Spain, for a sabbatical visit to Haldor Topsøe A/S.

**Competing interests statement** The authors declare competing financial interests: details accompany the paper on **www.nature.com/nature**.

**Correspondence** and requests for materials should be addressed to S.H. (sth@topsoe.dk).

# Enhanced ice sheet growth in Eurasia owing to adjacent ice-dammed lakes

**G. Krinner[1], J. Mangerud[2], M. Jakobsson[3], M. Crucifix[4]*, C. Ritz[1] & J. I. Svendsen[2]**

[1]*LGGE, CNRS-UJF Grenoble, BP 96, F-38402 Saint Martin d'Hères, France*
[2]*Department of Earth Science, University of Bergen, and Bjerknes Centre for Climate Research, Allégt. 41, N-5007 Bergen, Norway*
[3]*Center for Coastal and Ocean Mapping/Joint Hydrographic Center, Chase Ocean Engineering Laboratory, 24 Colovos Road, Durham, New Hampshire 03824, USA*
[4]*Institut d'Astronomie et de Géophysique G. Lemaître, Université catholique de Louvain, chemin du Cyclotron, 2, B-1348 Louvain-la-Neuve, Belgium*

* Present address: Met Office, Hadley Centre for Climate Prediction and Research, Fitzroy Road, Exeter EX1 3PB, UK

**Large proglacial lakes cool regional summer climate because of their large heat capacity, and have been shown to modify precipitation through mesoscale atmospheric feedbacks, as in the case of Lake Agassiz[1]. Several large ice-dammed lakes, with a combined area twice that of the Caspian Sea, were formed in northern Eurasia about 90,000 years ago, during the last glacial period when an ice sheet centred over the Barents and Kara seas[2] blocked the large northbound Russian rivers[3]. Here we present high-resolution simulations with an atmospheric general circulation model that explicitly simulates the surface mass balance of the ice sheet. We show that the main influence of the Eurasian proglacial lakes was a significant reduction of ice sheet melting at the southern margin of the Barents–Kara ice sheet through strong regional summer cooling over large parts of Russia. In our simulations, the summer melt reduction clearly outweighs lake-induced decreases in moisture and hence snowfall, such as has been reported earlier for Lake Agassiz[1]. We conclude that the summer cooling mechanism from proglacial lakes accelerated ice sheet growth and delayed ice sheet decay in Eurasia and probably also in North America.**

We used the LMDZ3 (Laboratoire de Météorologie Dynamique, CNRS Paris) stretched-grid atmosphere general circulation model (AGCM). In addition to a present-day reference simulation (called 'PD'), two simulations for 90 kyr before present (BP) were carried out. Both were constrained by appropriate ice sheet reconstructions, sea surface conditions, greenhouse gas concentrations and insolation as boundary conditions (Fig. 1; see Methods for details). They


©2004 Nature Publishing Group

differ by the fact that experiment 'L' (for 'lakes') includes Russian ice-dammed lakes[3] and the Baltic lake[4], while these are replaced by normal continental surface in simulation 'NL' (for 'no lakes'). The grid-stretching capability of LMDZ3 allows high resolution (100 km) over the Barents–Kara region. Compared with observed present-day surface air temperature[5] and precipitation[6], the mean absolute annual temperature error in simulation PD over the region of interest is fairly low (1.0 °C), but annual precipitation is overestimated by about 60%, mainly because of a wet bias in winter. On the other hand, LMDZ3 quite adequately captures the present surface mass balance patterns and quantities over the present ice sheets[7,8].

Analysis of the upper soil temperatures in the region in simulation L, based on a normalized surface frost index[9], shows that the Russian proglacial lakes were mostly situated within the limit of continuous permafrost, only the southernmost part of the West Siberian Lake (Fig. 1) extending into a region with extensive discontinuous permafrost. This is in agreement with ice wedge casts found on palaeo-beaches[10]. In both L and NL, simulated precipitation 90 kyr ago is less than 50% of PD over large parts of Russia. Simulated inflow of ice sheet melt water is substantial in L, corresponding to more than 1 m $yr^{-1}$ lake level rise. This is supported by findings of ice marginal deltas formed in the lakes[11]. Simulated lake summer surface temperatures exceed 4 °C only near the southern shore. In their northern parts, the proglacial lakes are cold monomictic (one vertical mixing per year, in summer; bottom temperature below 4 °C). They remain ice-covered from 7 months per year on the southern shore to 11 months per year near the ice sheet in spite of high meltwater input rates. The Baltic Lake, situated at lower latitudes, is somewhat warmer, and the ice cover lasts between 6 months on the southern shore and 9 months near the ice sheet. During all seasons, surface winds over the ice sheet in L and NL show a typical katabatic pattern, the air masses flowing down the slope of the ice sheet, deviated to the right because of the Earth's rotation, with maximum speeds near the ice sheet margin.

The primary atmospheric effect of the lakes is a strong summer cooling due to their large heat capacity. Summer surface air temperature anomalies (L–NL) exceed −10 °C above the lakes. The impact over the southern margin of the Barents–Kara ice sheet is substantial up to an altitude of about 2,000 m (Fig. 2a). This cooling effect extends horizontally about 1,000 km away from the lakes. The accumulation of cool air off and above the ice sheet margin decreases the horizontal air density gradient, and therefore induces a weakening of the katabatic circulation in summer. Above the lakes, the summer cooling is associated with a substantial surface pressure increase (+4 mbar). The summer cooling, and, to a lesser degree, the reduced surface wind speed on the ice sheet slope (leading to lower downward turbulent surface heat fluxes), strongly reduce summer melt along the southern margin of the Barents–Kara ice sheet and the southeastern margin of the Scandinavian ice sheet. On the lakeward parts of the ice sheet, runoff is reduced by 8 mm $d^{-1}$ in July, and by more than 500 mm $yr^{-1}$ (50%) in the annual mean, when the lakes are taken into account (refreezing of melt water is accounted for in calculating runoff from snow and ice melt[12]). Sensitivity tests showed that both the sign and the absolute value of the annual mean precipitation change are dependent on the prescribed sea-surface boundary conditions, but the precipitation change always remains far smaller than the ablation decrease. The latter coherently dominates the simulated surface mass balance change (Fig. 2b).

The Barents–Kara and the Scandinavian ice sheets were linked by a relatively small ice bridge at about 35 °E. Their surface mass balances (SMB, Fig. 3) are therefore analysed separately. The integrated SMB of the Barents–Kara ice sheet, defined as precipitation minus evaporation/sublimation and minus runoff, is +0.18 m of water equivalent per year ($m_w\,yr^{-1}$) in L, and −0.43 $m_w\,yr^{-1}$ in NL. According to a paired Student's *t*-test with nine degrees of freedom, the confidence in the SMB increase in L with respect to NL exceeds 99%, which excludes our result from being an artefact of interannual variability. Furthermore, the southern ablation zone of the Barents–Kara ice sheet extends over

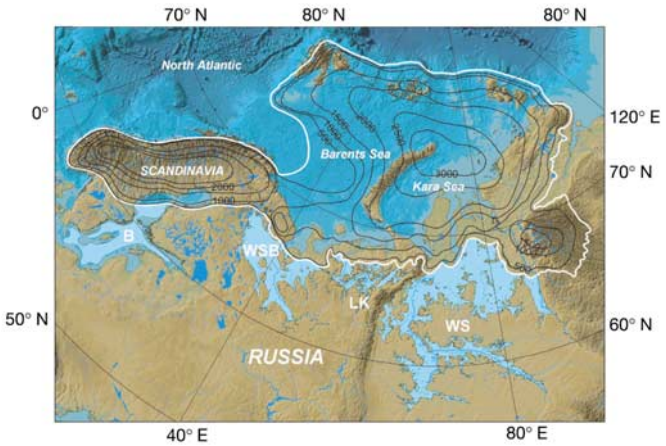


**Figure 1** Maximum ice sheet and lake extent in northern Russia during the early Weichselian, about 90,000 yr ago. Abbreviations denote the West Siberian Lake (WS), Lake Komi (LK), the White Sea Basin Lake (WSB), and the Baltic Lake (B).

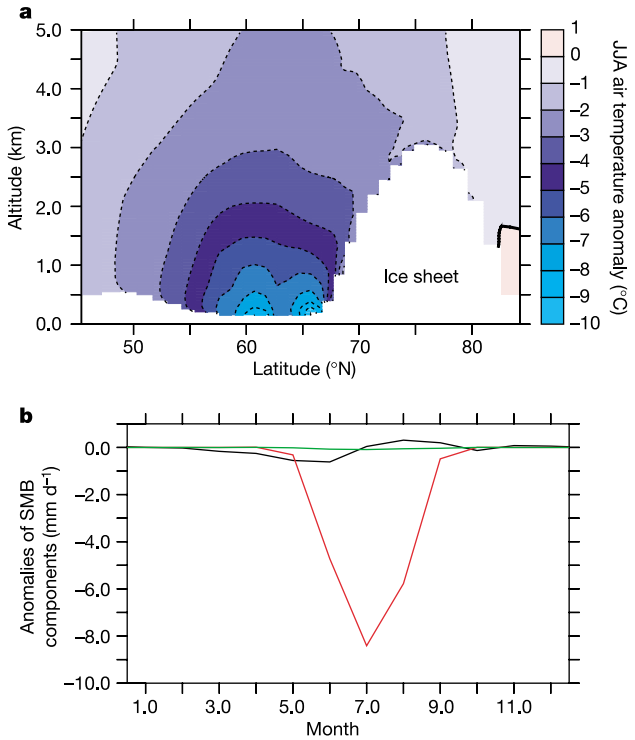


**Figure 2** Lake-induced climate anomalies between simulation L and simulation NL. **a**, JJA (June, July, August) air temperature anomalies: vertical cut through the lower atmosphere at 70° E. The pattern is representative for all longitudes where proglacial lakes are adjacent to the Barents–Kara ice sheet. **b**, Monthly mean anomalies of surface mass balance (SMB) components precipitation (black), runoff (red) and evaporation/sublimation (green) on the Scandinavian/Barents–Kara ice sheet grid points that belong to the lakes' drainage basin.


©2004 Nature Publishing Group

several grid points towards the interior in simulation NL, and significant melt (in excess of 0.2 $m_w\,yr^{-1}$) occurs in both simulations at least two grid points from the ice limit. Hence, the resolution is sufficient to capture melt processes, such that the sensitivity of the SMB can be better trusted than in most AGCMs that hardly represent the ablation zone. Concerning the Scandinavian ice sheet, the Russian proglacial lakes and the Baltic Lake induce a substantial increase (+1.7 $m_w\,yr^{-1}$) of the simulated SMB owing to reduced melt rates. Note that the prescribed western margin of the Scandinavian ice sheet does not reach the Atlantic coastline, and that outlet glaciers in fjords and valleys are not prescribed, owing to insufficient resolution. The westernmost ice sheet grid points are therefore at altitudes (more than 1,000 m, mostly more than 1,500 m) where significant ablation does not occur, which explains the high surface mass balance obtained here. High melt rates and therefore negative surface mass balances are simulated on a few low-altitude grid points near Franz Josef Land. Given the high latitude, the great distance to the Atlantic, the vicinity of the glacial Arctic Ocean, the ice sheet to the south, and low $CO_2$ concentrations, this result seems unlikely.

Although it focused on a different climatic and regional context, it is interesting to note that a study of the North American climate at 11,000 yr BP (ref. 1) suggested that the presence of proglacial Lake Agassiz caused a reduction of precipitation rates on the adjacent Laurentide ice sheet (the magnitude of which is similar to the precipitation changes induced by the Russian proglacial lakes, and much weaker than the ablation reduction reported here). The authors concluded that this precipitation reduction led to a decreased surface mass balance of the Laurentide ice sheet. However, assessing the surface mass balance precisely was not possible in that study as ice melt was not explicitly calculated (S. W. Hostetler, personal communication). Because the same study suggested that Lake Agassiz induced a significant regional cooling in summer, similar to the cooling induced by the Russian lakes reported here, we postulate that the lake-induced reduction in melting on the southern margin of the Laurentide ice sheet was larger than the reduction of precipitation. Furthermore, we see no reason why the feed-back mechanism reported here should not have operated during earlier growth and decay phases of the Laurentide ice sheet, during which large ice-dammed lakes are known to have existed[13].

The main conclusion of this study is that the Russian proglacial lakes, through their effect on the surface mass balance of the Barents–Kara ice sheet, repeatedly played an important role in the regional climate dynamics. Inception of the Barents–Kara ice sheet was probably caused by insolation changes and positive feedbacks involving snow albedo, ocean circulation[14], vegetation[15,16] and greenhouse gas concentration changes[17]. As soon as the ice sheet was big enough to dam the northward flowing Russian rivers, thereby creating the proglacial lakes, this initial growth of the Barents–Kara ice sheet was notably enhanced. Optical stimulated luminescence dates indicate that the ice sheet attained its maximum extent between 90 and 80 kyr ago[2,10]. On the other hand, June insolation at 65 °N, which is close to the southern limit of the Barents–Kara ice sheet, increased by ~12% between 95 and 85 kyr ago[18]. The most coherent scenario is therefore that the ice sheet attained its maximum extent at about 90 kyr ago, and that a subsequent retreat (delayed, but not stopped by the lake-induced melt reduction) began around 85 kyr ago owing to increased summer insolation. Once the Barents–Kara ice sheet had shrunk sufficiently, rapid subglacial drainage of the lakes occurred. This further accelerated the deglaciation by leading to higher summer melt rates along the southern ice sheet margin.

Note that rapid drainage of proglacial lakes along the southern margin of the Laurentide ice sheet is thought to have caused abrupt widespread cooling by interrupting the oceanic thermohaline circulation[19]; it has been suggested that a similar cooling, possibly compensating for the regional warming caused by the drainage of the lakes, might have occurred following lake drainage in northern Eurasia[11]. During later stages of the last glacial, in particular the Last Glacial Maximum (about 20,000 yr ago), the Barents–Kara ice sheet did not grow big enough to create large proglacial lakes[11] (possibly because the larger Scandinavian ice sheet blocked moisture delivery from the Atlantic), and the growth acceleration due to these lakes therefore did not take place. Finally, we note that the coupled lake–ice sheet system could be self-sustaining to a certain degree: a small ice sheet decay leads to an increased lake size, thereby cooling the climate and thus reducing the meltwater production. This negative feedback will break down if the ice sheet decay is sufficiently pronounced to allow drainage of the lake through previously blocked passages. □

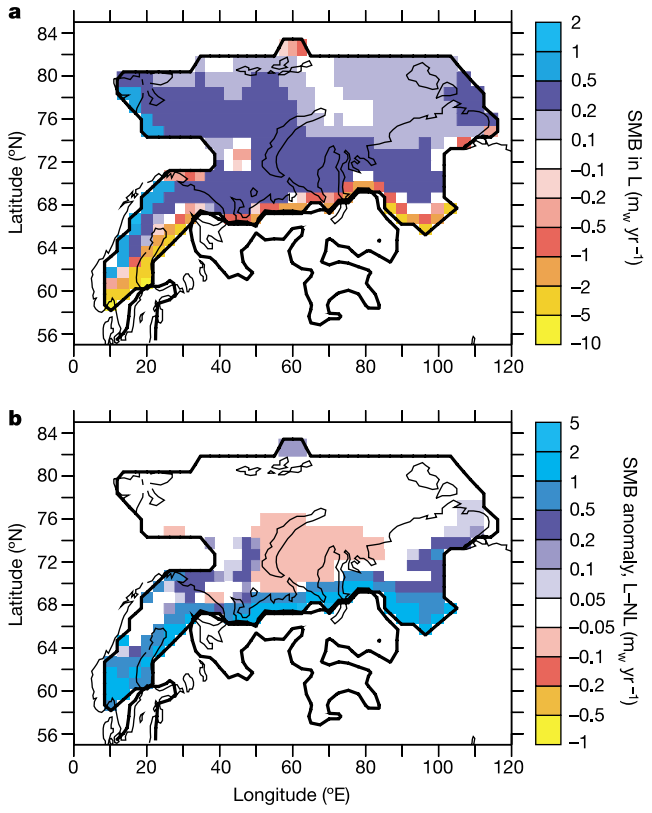


**Figure 3** Simulated ice sheet surface mass balance and lake-induced surface mass balance anomaly. **a**, Simulated surface mass balance in simulation L; **b**, lake-induced anomaly (L–NL). Units are metres of water equivalent per year. Bold lines, ice sheets and lakes (grid-scale fraction > 20%) for 90 kyr ago; thin line, present-day coastline.

## Methods

### Model

The LMDZ3 model has been run with 96 × 72 (longitude × latitude) grid points. The chosen nominal horizontal resolution is irregular, varying from 100 km at the centre of the region of interest (between 0° and 120 E and between 55° and 85° N) to about 550 km roughly at the antipodes of this region. The model has 19 vertical layers in the atmosphere. LMDZ3 has been adapted for the simulation of cold climates[20] and includes a thermal lake module[21].

### Boundary conditions

The prescribed boundary conditions (Fig. 1) for the AGCM include orbital parameters for 90 kyr ago[18]; an atmospheric $CO_2$ concentration of 205 p.p.m.v. (ref. 22); reconstructed dimensions of the Barents–Kara and the Scandinavian ice sheet based on geological evidence[2] and glaciological modelling[23] with some modifications to fit the latest results


©2004 Nature Publishing Group

obtained within the ESF-QUEEN project; ice sheet thicknesses for the rest of the Northern Hemisphere obtained using the climatic index method[24] applied to an ice sheet model and AGCM outputs[25]; modelled global sea surface temperatures and sea-ice extent[26], surface albedo and roughness over ice-free surfaces derived from modelled glacial maximum palaeovegetation[27]; a large lake in the part of the Baltic Sea depression not covered by the Scandinavian ice sheet[4]; and reconstructed proglacial lakes in European Russia and in West Siberia[3].

### Initial conditions and spin-up

The simulations were started from an initial state with present-day soil temperatures. From the 15 yr of each simulation, the first five years were discarded as spin-up. Lake temperatures at the bottom level (between 15 and 30 m) were in equilibrium at the end of the 5 spin-up years. At the end of each of the first three spin-up years for the 90-kyr-ago simulations, soil temperature, being the slowest simulated component of the climate system simulated here, was separately spun up for 1,000 yr using the year's modelled monthly surface temperatures.

Received 15 May; accepted 14 November 2003; doi:10.1038/nature02233.


1. Hostetler, S. W., Bartlein, P. J., Clark, P. U., Small, E. E. & Solomon, A. M. Simulated influences of Lake Agassiz on the climate of central North America 11,000 years ago. *Nature* **405,** 334–337 (2000).
2. Svendsen, J. I. *et al.* Late Quaternary ice sheet history of Eurasia. *Quat. Sci. Rev* (in the press).
3. Mangerud, J., Astakhov, V., Jakobsson, M. & Svendsen, J. I. Huge ice-age lakes in Russia. *J. Quat. Sci.* **16,** 773–777 (2001).
4. Lundquist, J. Glacial stratigraphy in Sweden. *Spec. Pap. Geol. Surv. Finl.* **15,** 43–59 (1992).
5. Legates, D. R. & Willmott, C. J. Mean seasonal and spatial variability in global surface air temperature. *Theor. Appl. Climatol.* **41,** 11–21 (1990).
6. Legates, D. R. & Willmott, C. J. Mean seasonal and spatial variability in gauge-corrected, global precipitation. *Int. J. Climatol.* **10,** 111–127 (1990).
7. Genthon, C. & Krinner, G. Antarctic surface mass balance and systematic biases in general circulation models. *J. Geophys. Res.* **106,** 20653–20664 (2001).
8. Krinner, G. & Werner, M. Impact of precipitation seasonality changes on isotopic signals in polar ice cores: A multi-model analysis. *Earth Planet. Sci. Lett.* **216,** 525–538 (2003).
9. Nelson, F. & Outcalt, S. I. A computational method for prediction and regionalization of permafrost. *Arct. Alp. Res.* **19,** 279–288 (1987).
10. Mangerud, J., Astakhov, V., Murray, A. & Svendsen, J. I. The chronology of a large ice-dammed lake and the Barents–Kara ice sheet advances, Northern Russia. *Glob. Planet. Change* **31,** 321–336 (2001).
11. Mangerud, J. *et al.* Ice-dammed lakes and rerouting of the drainage of northern Eurasia during the last glaciation. *Quat. Sci. Rev.* (in the press).
12. Thompson, S. L. & Pollard, D. Greenland and Antarctic mass balances for present and doubled atmospheric $CO_2$ from the GENESIS version-2 global climate model. *J. Clim.* **10,** 871–900 (1997).
13. Teller, J. T. in *The Quaternary Period in the United States* (eds Gillespie, A., Porter, S. & Atwater, B.) Ch. 3 (Elsevier, Amsterdam, 2003).
14. Khodri, M. *et al.* Simulating the amplification of orbital forcing by ocean feedbacks in the last glaciation. *Nature* **410,** 570–574 (2001).
15. de Noblet, N. *et al.* Possible role of atmosphere-biosphere interactions in triggering the last glaciation. *Geophys. Res. Lett.* **23,** 3191–3194 (1996).
16. Gallimore, R. G. & Kutzbach, J. E. Role of orbitally induced changes in tundra area in the onset of glaciation. *Nature* **381,** 503–505 (1996).
17. Shackleton, N. J. The 100,000-year ice-age cycle identified and found to lag temperature, carbon dioxide, and orbital eccentricity. *Science* **289,** 1897–1902 (2000).
18. Berger, A. Long-term variations of daily insolation and Quaternary climatic changes. *J. Atmos. Sci.* **35,** 2362–2367 (1978).
19. Clarke, G., Leverington, D., Teller, J. & Dyke, A. Superlakes, megafloods, and abrupt climate change. *Science* **301,** 922–923 (2003).
20. Krinner, G., Genthon, C., Li, L. & Le Van, P. Studies of the Antarctic climate using a stretched-grid general circulation model. *J. Geophys. Res.* **102,** 13731–13745 (1997).
21. Krinner, G. Impact of lakes and wetlands on boreal climate. *J. Geophys. Res. D* **108,** 101029/2002JD002597 (2003).
22. Petit, J.-R. *et al.* Climate and atmospheric history of the past 420,000 years from the Vostok ice core, Antarctica. *Nature* **399,** 426–436 (1999).
23. Siegert, M. J., Dowdeswell, J. A., Hald, M. & Svendsen, J. I. Modelling the Eurasian ice sheet through a full (Weichselian) glacial cycle. *Glob. Planet. Change* **31,** 367–385 (2001).
24. Marshall, S. J., Tarasov, L., Clarke, G. & Peltier, W. R. Glaciological reconstruction of the Laurentide Ice Sheet: Physical processes and modelling challenges. *Can. J. Earth Sci.* **37,** 769–793 (2000).
25. Charbit, S., Ritz, C. & Ramstein, G. Simulations of Northern Hemisphere ice-sheet retreat: Sensitivity to physical mechanisms involved during the Last Deglaciation. *Quat. Sci. Rev.* **21,** 243–266 (2002).
26. Crucifix, M., Loutre, M. F., Tulkens, P., Fichefet, T. & Berger, A. Climate evolution during the Holocene: a study with an Earth system model of intermediate complexity. *Clim. Dyn.* **19,** 43–60 (2002).
27. Crowley, T. Ice age terrestrial carbon changes revisited. *Glob. Biogeochem. Cycles* **9,** 377–389 (1995).


**Acknowledgements** We thank S. Hostetler for discussions and M. Siegert for comments and suggestions. Model simulations were carried out at IDRIS/CNRS. This work was supported by the ESF and the French national programmes ECLIPSE, PNEDC and ACI Jeunes Chercheurs. The field work and other analyses were funded by the Research Council of Norway by grants to the PECHORA project. M.J. was supported by NOAA.

**Competing interests statement** The authors declare that they have no competing financial interests.

**Correspondence** and requests for materials should be addressed to G.K. (krinner@ujf-grenoble.fr).

# Natural examples of olivine lattice preferred orientation patterns with a flow-normal *a*-axis maximum

**Tomoyuki Mizukami[1,2], Simon R. Wallis[2] & Junji Yamamoto[3]***

[1]*Department of Geology and Mineralogy, University of Kyoto, Sakyo-ku, Kyoto, 606-8501, Japan*
[2]*Department of Earth and Planetary Sciences, Graduate School of Environmental Studies, University of Nagoya, Chikusa-ku, Nagoya, 464-8601, Japan*
[3]*Laboratory of Earthquake Chemistry, University of Tokyo, Bunkyo-ku, Tokyo, 113-0033, Japan*

* Present address: Department of Earth and Planetary Sciences, Tokyo Institute of Technology, Meguro-ku, Tokyo, 152-8551, Japan

**Tectonic plate motion is thought to cause solid-state plastic flow within the underlying upper mantle and accordingly lead to the development of a lattice preferred orientation of the constituent olivine crystals[1–3]. The mechanical anisotropy that results from such preferred orientation typically produces a direction of maximum seismic wave velocity parallel to the plate motion direction[4,5]. This has been explained by the existence of an olivine preferred orientation with an '*a*-axis' maximum parallel to the induced mantle flow direction[3,5,6–8]. In subduction zones, however, the olivine *a* axes have been inferred to be arranged roughly perpendicular to plate motion[9–13], which has usually been ascribed to localized complex mantle flow patterns[10–13]. Recent experimental work[14] suggests an alternative explanation: under conditions of high water activity, a 'B-type' olivine preferred orientation may form, with the *a*-axis maximum perpendicular to the flow direction. Natural examples of such B-type preferred orientation are, however, almost entirely unknown. Here we document widespread B-type olivine preferred orientation patterns from a subduction-type metamorphic belt in southwest Japan and show that these patterns developed in the presence of water. Our discovery implies that mantle flow above subduction zones may be much simpler than has generally been thought.**

The Higashi-akaishi peridotite body of southwest Japan is the only kilometre-scale garnet peridotite body yet found in a subduction-type metamorphic belt[15]. This body offers an unrivalled opportunity to study subduction zone mantle directly. Here we focus on the olivine lattice preferred orientation (LPO) patterns of this body. The Higashi-akaishi body is tabular with an area of 10 $km^2$ and a thickness of 500 m (ref. 16) and occurs as an integral part of the Cretaceous Sanbagawa high-pressure, low-temperature metamorphic belt[17–19]. Dunite, a rock type of more than 90% olivine, is the main constituent of the body with minor amounts of wehrlite, pyroxenite, garnet pyroxenite, chromitite and garnet peridotite[15,16,20]. Serpentinized equivalents of these rock types developed in the periphery of the body[14] during exhumation, but the earlier olivine-rich microstructures and associated petrological information are well preserved in the inner part (Figs 1, 2).

Field observations and microstructural analyses allow two generations of tectonic fabrics to be distinguished in the dunite. The earliest $D_1$ fabric is defined by the crystal-shape preferred orientation of coarse clear olivine grains (~0.6 mm) (Fig. 1a). A second $D_2$ fabric is widespread throughout the Higashi-akaishi body and consists of coarse dusty olivine porphyroclasts (~0.5 mm) and fine clear olivine neoblasts (~0.1 mm) (Fig. 1c), which formed by dynamic recrystallization of the $D_1$ coarse-grained fabric (Fig. 1d). The preferred alignment of olivine crystals defines planar and linear fabrics for both $D_1$ (Fig. 1a) and $D_2$ (Fig. 1c). The olivine grain shape lineations are interpreted to be parallel to the maximum extension direction. This interpretation is supported by the com-


©2004 Nature Publishing Group